Available online at www.sciencedirect.com
ScienceDirect
Combustion and Flame 151 (2007) 333–346
Combustion and Flame
www.elsevier.com/locate/combustflame

Diesel combustion: In-cylinder NO concentrations in relation to injection timing

K. Verbiezen [a], A.J. Donkerbroek [a], R.J.H. Klein-Douwel [a], A.P. van Vliet [a], P.J.M. Frijters [b], X.L.J. Seykens [b], R.S.G. Baert [b], W.L. Meerts [a], N.J. Dam [a,*], J.J. ter Meulen [a]

[a] *Institute for Molecules and Materials, Applied Physics, Radboud University of Nijmegen, Toernooiveld 1, 6525 ED Nijmegen, The Netherlands*
[b] *Mechanical Engineering, Eindhoven University of Technology, P.O. Box 513, WH 3.143, 5600 MB Eindhoven, The Netherlands*

Received 15 January 2007; received in revised form 6 May 2007; accepted 12 May 2007

Available online 28 June 2007

Abstract

This paper presents local experimental in-cylinder concentrations of nitric oxide, obtained by laser-induced fluorescence measurements in a heavy-duty diesel engine. Quantitative concentration histories during the entire combustion stroke are shown for a number of fuel injection timings. Using images from high-speed combustion visualization experiments, the presence of the diffusion flame is related to the onset of NO formation within the laser probe volume. Further attention is paid to the possible NO formation mechanisms. Off-line characterization of the fuel sprays by means of Schlieren imaging reveals that the initial (premixed) combustion is too fuel-rich for thermal (Zeldovich) NO formation. Furthermore, the experimental NO concentrations are compared to numerical calculations of the thermal NO formation during the mixing-controlled combustion phase. The agreement between model and experiments suggests that the thermal mechanism is the major NO formation pathway. However, it cannot be excluded that transport to the probe volume of early NO, formed under conditions where the thermal mechanism is ineffective, might be of some importance as well.

Keywords: NO formation; Diesel engine; Laser-induced fluorescence

1. Introduction

Despite their superior efficiency and resulting low fuel consumption and CO_2 emissions, diesel engines are notorious for their relatively levels of high emission of particulate matter (PM) and NO_x. Optimizing the combustion process (i.e., reducing NO_x and PM emissions without serious compromises in fuel consumption and emissions of CO and unburnt hydrocarbons) requires profound knowledge of all formation processes involved. Diesel combustion models need support from numerical and/or experimental data. Whereas three-dimensional numerical simulations of extremely complex processes such as diesel combustion are computationally very expensive, the

* Corresponding author.
E-mail address: n.dam@science.ru.nl (N.J. Dam).

0010-2180/$ – see front matter
doi:10.1016/j.combustflame.2007.05.005

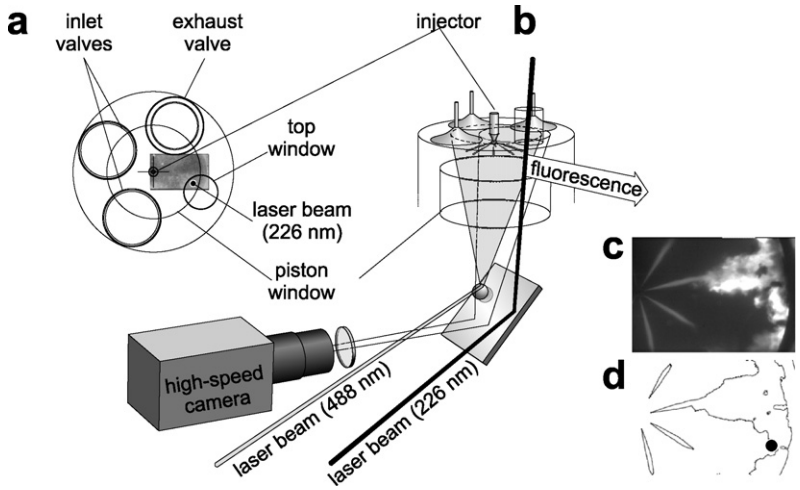

Fig. 1. Schematic representation of the engine setup: (a) top view, indicating the field of view of the high-speed camera and the NO LIF probe position; (b) three-dimensional view of the measurement cylinder; (c) 23-μs snapshot of the combusting fuel sprays, as recorded by the high-speed camera at 6.3° aTDC (start of injection = 8° bTDC); (d) contour plot of the same image, indicating the laser probe location (black dot). The 226-nm laser beam traverses the cylinder almost parallel to its axis. NO fluorescence is detected by an imaging grating spectrograph (not shown) through the nearest side window.

challenge on the experimental side is to develop reliable measurement techniques.

Here, we focus on the formation of nitric oxide (NO), presenting quantitative local in-cylinder NO concentration histories as measured by laser-induced fluorescence (LIF) in a DI diesel engine. Although the LIF technique has often been applied for NO measurements in diesel engines [1–7], the severe attenuation of the laser beam and the induced fluorescence is not always properly addressed. Exceptions are Stoffels et al. [4], who measured spatially resolved laser beam transmission (although no correction was made for the attenuation of the NO fluorescence), and Hildenbrand et al. [7], who corrected for the absorption of NO fluorescence by CO_2 (but neglecting additional LIF attenuation caused by, e.g., soot, and lacking a correction for laser beam attenuation). Recently we investigated a number of attenuation correction methods, the combination of which yields a complete picture of all major attenuation processes involved in NO LIF measurements in a diesel engine [8]. This detailed correction strategy has allowed for the first time a quantitative measurement of the NO concentration in a heavy-duty diesel engine [9].

In this paper, we present in-cylinder NO concentration histories for a number of fuel injection timings. Although the effect of injection timing on the exhaust NO concentration is well known, quantitative in-cylinder measurements are scarce. In order to interpret our data within the framework of current ideas on diesel spray combustion [10–12], a further characterization of the combustion process is indispensable. In a joint effort of research groups in Nijmegen and Eindhoven, the NO LIF data are complemented by additional experiments including high-speed combustion visualization (in the same research engine) and Schlieren imaging of the fuel injection (in a high-pressure cell) and by NO chemistry modeling.

2. Experiment

2.1. The engine

The research engine is a six-cylinder, heavy-duty diesel truck engine. One of its cylinders (hereafter referred to as "measurement cylinder") is optically accessible via fused silica windows in the piston ("piston window"), in the cylinder wall ("side windows"), and in the cylinder head ("top window"). A slot machined into the piston crown prevents blocking of the detection side window around top dead center (TDC). The measurement cylinder is depicted schematically in Fig. 1, and its most relevant specifications are compiled in Table 1. For measurements of the cylinder pressure, the top window can be replaced by a pressure transducer (AVL QHC32). An eight-hole fuel injector is mounted centrally and can be rotated for easy alignment of the fuel spray with respect to the laser beam probe volume. Fuel injection into the measurement cylinder is provided by a home-built common-rail system. The start and end of the injection can be set independently via the electronically actuated injector, each injection yielding 60 mg at 1200 bar. Fig. 2 shows the rail pressure during an injection event. During the injection, the pressure varies by

Table 1
Specifications and global operating conditions of the measurement cylinder

Engine type	Six-cylinder four-stroke DI diesel engine
Bore, stroke	130 mm, 146 mm
Displacement	1.939 L (per cylinder)
Compression ratio	15 (unmodified: 16)
Piston bowl shape	"Bathtub" (flat piston window)
∅ piston bowl	84 mm
Swirl number	1.8
∅ injector, # holes	0.128 mm, 8
Fuel injected, inj. pressure	60 mg of low-sulfur diesel, 1200 bar
Boost pressure	1.4 bar (abs.; no EGR)
Engine speed	1430 rpm

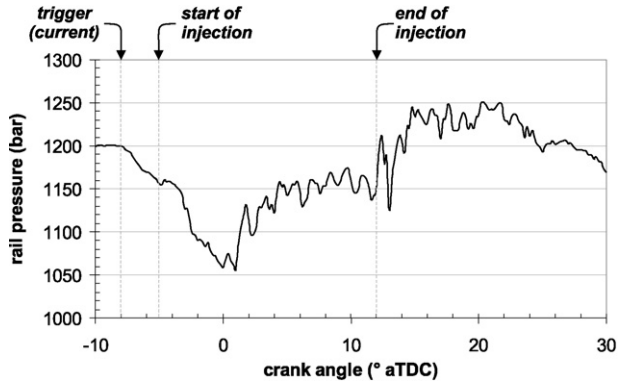

Fig. 2. Typical injection pressure trace for the engine experiments. For the data shown here, the injector is actuated at 8° bTDC, as is indicated by the arrow. The actual start and end of injection are indicated as well.

∼12%. The electronics also allows a double (split) fuel injection (see Appendix A). The oil-free measurement cylinder is skip-fired (1:35) to avoid overheating; three unmodified cylinders are continuously fueled (by the original line pump) to maintain engine speed.

Measurements were conducted with a rail pressure of 1200 bar and at four different fuel injection timings, actuating the fuel injector at 18°, 13°, 8°, and 3° bTDC (bTDC = before TDC). The *effective* start of injection (SoI_{eff}) was determined from high-speed imaging (see Section 2.2) and occurs about 3° later; see Table 2 for details. Unless explicitly stated otherwise, SoI means the *nominal* start of injection (i.e. actuation of the injection system). The start of combustion was retrieved from the cylinder pressure trace and the derived rate of heat release [13], shown in Fig. 3.

2.2. High-speed combustion visualization

The combustion process was recorded through the piston window by a high-speed camera (Phantom V7.1, 160 kHz maximum frame rate); see Fig. 1. To visualize the fuel sprays prior to combustion, a continuous-wave argon ion laser beam (Spectra Physics, Stabilite 2016) of circa 5 W (operating primarily at 488 and 517 nm) was directed toward a 16-mm-diameter metal sphere located below the piston window, resulting in a highly divergent reflection illuminating almost the entire combustion chamber. To avoid overexposure of the camera and to suppress the combustion light, a filter combination (BG 18 and GG 475 Schott filters) was used, transmitting roughly between 460 and 640 nm. The camera was synchro-

Table 2
Operating points of the measurement cylinder[a]

SoI (nominal)	−18.0°	−13.0°	−8.0°	−3.0°
SoI_{eff} (effective)	−14.8°	−9.3°	−4.5°	0.3°
EoI	0.6°	6.0°	11.1°	15.8°
SoC	−8.9°	−5.5°	0.4°	4.2°
Inj. duration	15.3°	15.3°	15.6°	15.5°
Ignition delay	5.9°	3.8°	4.1°	3.9°
gIMEP (kPa)	502 ± 6	509 ± 4	496 ± 11	498 ± 1
$[NO]_{exhaust}$ (ppm)	560 ± 112	402 ± 80	272 ± 55	190 ± 38

[a] All crank angles in ° aTDC (aTDC = after TDC; SoI = start of injection; EoI = end of injection; SoC = start of combustion).

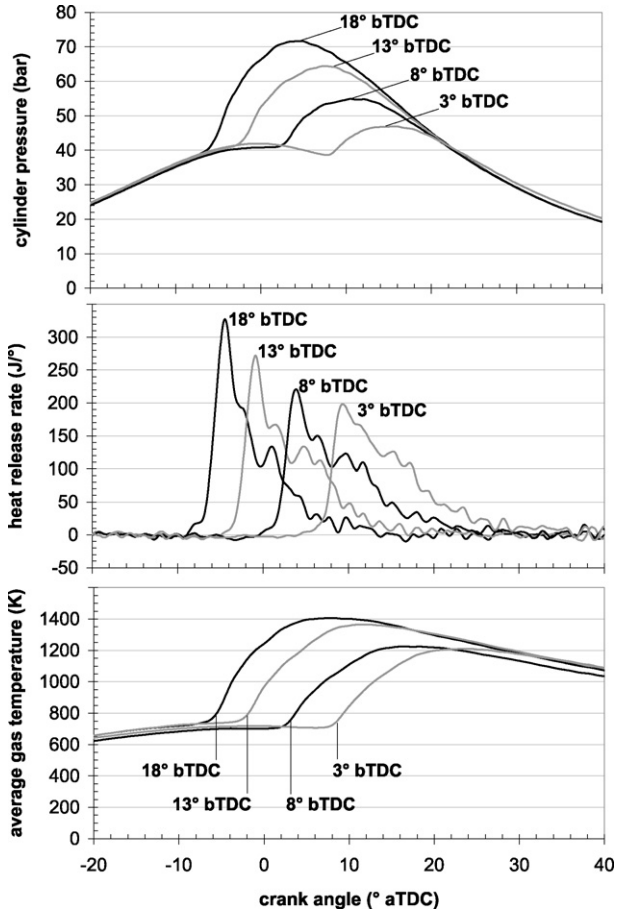

Fig. 3. Cylinder pressure (top), rate of heat release (middle), and average gas temperature (bottom) for the four injection timings. The nominal start of injection is indicated for each curve.

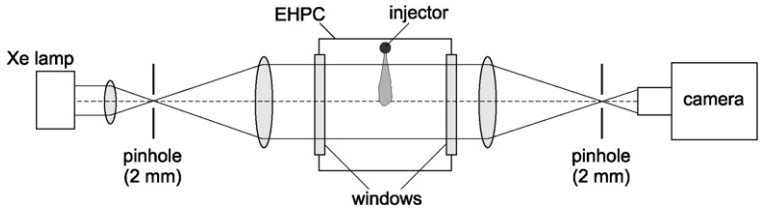

Fig. 4. The Schlieren imaging setup including the Eindhoven high-pressure, high-temperature cell (EHPC).

nized to the crankshaft of the engine and recorded at one image every 0.3° CA (∼35 μs), with an exposure time of 23 μs, and a resolution of 275 μm per pixel.

2.3. Fuel spray imaging

The laser elastic scattering measurements merely visualize the liquid phase of the spray (including droplets). Additional off-line experiments involving Schlieren imaging were carried out to image the fuel vapor as well. The Schlieren technique is particularly sensitive to variations in the index of refraction, and hence to density gradients, which allows a better characterization of the spray geometry. These measurements were performed in the Eindhoven high-pressure, high-temperature cell (EHPC) using the same injector type and rail pressure as in the engine experiments. A schematic representation of the Schlieren setup is shown in Fig. 4.

Vaporizing conditions (30.9 bar and 770 K) were realized by igniting a combustable mixture 2500 ms prior to the fuel injection. After this precombustion,

an inert hot gas mixture (N_2, CO_2, and H_2O) with a density of 14 kg/m^3 remains. In addition, multiple series of injection events were visualized in a colder (473 K) inert ambient gas. Various ambient densities (15–25 kg/m^3) were studied, covering the range found in the engine tests. These tests furthermore showed that the sprays from different nozzle holes were very similar, as was also confirmed by the high-speed visualization experiments on the test engine. Further details of the EHPC can be found in Refs. [14,15].

For these measurements the same Phantom camera was used, operating at 60.7 kHz, with an exposure time of 2 μs, and a resolution of 430 μm per pixel.

2.4. NO LIF measurements

The laser beam for NO excitation traverses the combustion chamber (almost) vertically, 30 mm away from the injector, and rotated over 26° in the swirl direction with respect to a fuel spray. The trajectory of the laser beam is shown in Fig. 1. The height of the probe volume is limited to the uppermost 23 mm of the combustion chamber by the size of the detection window.

NO LIF is induced by laser radiation at 226.03 nm, resonant with the coinciding $A^2\Sigma(v' = 0) \leftarrow X^2\Pi(v'' = 0)$ $P_1(23.5)$, $Q_1 + P_{21}(14.5)$, and $Q_2 + R_{12}(20.5)$ transitions. This excitation wavelength was suggested by diRosa et al. [17] for high sensitivity and minimal O_2 LIF interference even at elevated pressures. Laser radiation (pulses of 5–8 mJ) is produced by a frequency-mixed dye laser (Radiant Narrowscan D) pumped by a Nd:YAG laser (Continuum Powerlite Precision II 8010). Four vibronic fluorescence bands (at 237, 248, 259, and 270 nm, corresponding to the $A \rightarrow X$ (0, 1)–(0, 4) transitions, respectively) are detected through the nearest side window by an intensified CCD camera (Roper Scientific, ICCD 512T, 512^2 pixels, 16 bits) mounted behind a spectrograph (ARC SpectraPro 500i, 600 lines/mm grating). The entrance slit of the spectrograph is parallel to the laser beam direction, and opened to encompass the entire laser beam width for maximum intensity. Two typical raw NO LIF images are shown in Fig. 5.

Attenuation effects are minimized (but not negligible; see Ref. [16]) by keeping the in-cylinder path lengths of laser beam and fluorescence as short as possible (0–23 and 37 mm, respectively).

2.5. NO LIF data processing

In the current analysis, the total NO LIF intensity per vibronic emission band is determined by summing all relevant pixel intensities (areas indicated by dashed lines in Fig. 5b). Consequently, the data represent the average NO density within the probe volume (⌀ 4 mm, height 23 mm). Quantification of the LIF signal requires extensive postprocessing [8,9], which we describe here only briefly. The importance of taking due care of all factors that affect the experimentally obtained signals may be appreciated by realizing that the total conversion factor, from NO LIF data to NO mole fractions, varies by about three orders of magnitude over an engine cycle [9].

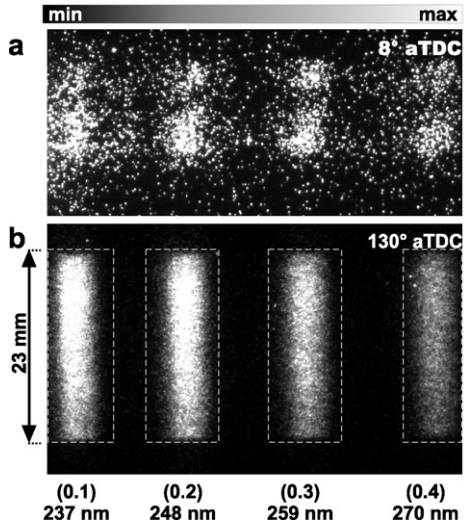

Fig. 5. Two single-shot NO LIF images (raw data) recorded through the side window by the spectrograph-camera system, at 8° aTDC (a) and 130° aTDC (b). The intensity scales are adjusted individually to show maximum contrast in each image. Start of injection: 8° bTDC.

2.5.1. Attenuation corrections

We have measured in-cylinder attenuation coefficients by means of (1) bidirectional LIF and (2) absorption spectroscopy of CO_2 and O_2. With bidirectional LIF, vertical NO LIF intensity profiles are measured for two opposite directions of the excitation laser beam; the spatially resolved laser beam transmission is calculated from the ratio of these profiles [18–21]. For a single-shot approach, the two counterpropagating laser pulses should be fired quasi-simultaneously. Here, all pulses are fired during different cycles, and thus we obtain averaged transmission data.

The attenuation of the NO fluorescence caused by absorption by CO_2 and O_2 can be obtained by comparing each measured NO LIF spectrum to a reference NO LIF spectrum (i.e., without absorption). The ratio of these spectra yields a relative transmission spectrum of the NO fluorescence on its way to the detector. Absolute transmission values are obtained by fitting this transmission spectrum, using parameterized CO_2

[22] and O_2 [23] absorption cross sections. Due to the strong temperature dependence of the CO_2 and O_2 absorption cross sections, each fit also yields an estimate for the local temperature[1] [24]. The additional attenuation of the NO fluorescence by, e.g., soot is estimated by comparing the calculated CO_2 and O_2 absorption (at 226 nm) to the (total) laser beam extinction as measured with bidirectional LIF.

We refer to Refs. [8,9] for a more complete description of these techniques and methodology. The above-mentioned technique has the advantage that it is performed simultaneously with the actual NO LIF measurements. Consequently, all measurements were carried out under identical conditions. Transmission curves for the laser beam and the fluorescence are presented in Ref. [16]. We apply phase-averaged correction factors to single-shot NO LIF data. The resulting NO concentrations are subsequently phase-averaged over 20 engine cycles in order to obtain statistics on cycle-to-cycle fluctuations. Error bars in the NO mole fractions presented below include both these cycle-to-cycle fluctuations and the uncertainties in the correction factors.

2.5.2. Pressure and temperature dependence

We have used LIFSim [25] to calculate the pressure and temperature dependence of the NO LIF intensity. Although the gas composition may have a large influence on the quenching rates and thus on the *absolute* LIF intensity, here we are only interested in the *relative* changes of the LIF signal (absolute values are obtained by calibration, see next paragraph). We have demonstrated previously that the exact gas composition is of minor importance [9], and all LIFSim calculations were performed for constant ($[O_2]$:$[N_2] = 1{:}4$) composition of the in-cylinder gases. Further input parameters were the cylinder pressure and the local temperature. The latter was estimated from the observed CO_2 and O_2 absorption spectra (previous paragraph).

2.5.3. Calibration

After correcting the NO LIF data for attenuation effects and the pressure and temperature dependence of the fluorescence yield, the processed data are multiplied by a calibration factor that scales the in-cylinder concentration at the end of the stroke (the exhaust valve opens at 130° aTDC) to the exhaust NO concentration. The latter is determined by a commercial exhaust gas analyser (SIGNAL Instruments, NOX analyzer series 4000), sampling the exhaust of only the measurement cylinder. Its reading is scaled by the skip-fire ratio and an additional factor accounting for the fact that the sampling occurs nonisokinetically (see Appendix B). We assume homogeneous phase-averaged NO distributions at 130° aTDC.

[1] In fact, the fitted temperature is a weighted average of the temperature profile along the trajectory of the NO fluorescence. This effective temperature is expected to be strongly biased to the probe volume temperature [9].

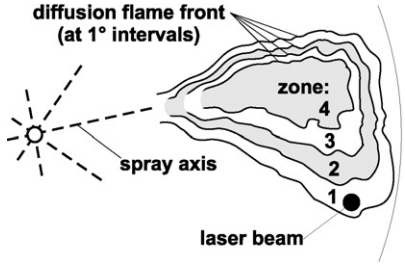

Fig. 6. Schematic representation of the combustion zones (numbered 1–4). The flame front is represented by solid lines; dashed lines indicate the spray axes; the position of the NO excitation laser beam is indicated by the black dot.

2.6. NO formation calculations

The thermal NO formation has been calculated using the extended Zeldovich mechanism. For the calculations, the combustion event is divided into steps of 1° CA, during which a certain amount of fuel is burnt. This divides the flame spatially into zones [26,27]. Each zone starts in the volume traversed by the flame front during the corresponding step of 1°. Subsequently, the zone moves outward as new zones are formed at the flame front during the following crank angle steps. This is shown schematically in Fig. 6. The calculations are based on the assumption that no mixing occurs between different zones; entrainment of fresh air into a zone, however, is modeled based on our spray visualization data that are used as input for the spray model by Naber and Siebers [10]. A chemical equilibrium solver (without N chemistry) [28] is used to calculate the composition of the combustion products and the corresponding adiabatic flame temperature. The latter is then used to calculate the thermally formed (Zeldovich) NO per zone. These calculations are detailed below.

The amount of fuel burnt in each zone (i.e. during 1°) is determined from the rate of heat release (Fig. 3). Only the mixing-controlled part of the combustion is considered (the premixed combustion is too fuel-rich for significant thermal NO formation, as will be discussed in Section 3.2). It is assumed that the combustion in each zone starts under stoichiometric conditions, which is a reasonable assumption for the diffusion flame. For each zone, the initial composition is now known. Its temperature is taken equal to the unburnt mixture temperature (derived from the pressure curve of the motored engine, without fuel injection), and is used as an input to a chemical equilibrium

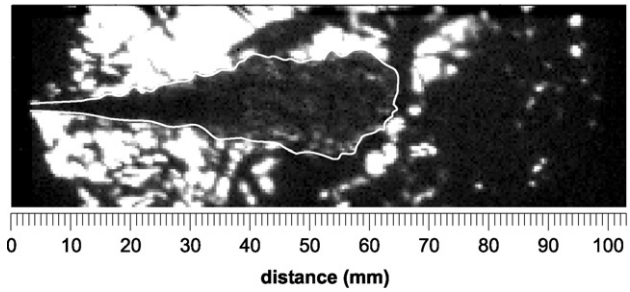

Fig. 7. Single frame from a high-speed Schlieren movie of a single fuel injection into the EHPC, at 770 K and 30.9 bar. The white contour guides the eye.

solver to determine the composition of the combustion products and the corresponding adiabatic flame temperature. Species considered are O_2, N_2, CO_2, H_2O, CO, H_2, OH, O, N, and H. In all zones, the pressure is equal to the measured in-cylinder pressure (Fig. 3).

With the adiabatic flame temperature and the O, O_2, N, OH, and H concentrations the NO formation rate is calculated by means of the extended Zeldovich mechanism. The main equations are

$$\frac{d[\mathrm{N}]}{dt} \approx 0, \tag{1}$$

$$\frac{d[\mathrm{NO}]}{dt} = 2k_{1,r}[\mathrm{O}][\mathrm{N}_2] - 2k_{1,l}[\mathrm{NO}][\mathrm{N}]. \tag{2}$$

The reaction rate constants k are taken from GRI 2.11 [29]. The zone temperature is initially equal to the adiabatic flame temperature, but it quickly decreases due to mixing with colder unburnt air and due to expansion of the cylinder volume. The resulting shift in the chemical equilibrium, influencing the NO formation rate, is included in the calculations. The computation of NO formation is stopped when the temperature of the zone drops below 1700 K, which is often used as a cutoff temperature for thermal NO formation.

3. Results and discussion

3.1. Engine characteristics

Table 2 summarizes the operating points that were used in this study. The effective start and end of injection were determined from the combustion movies measured in the engine. The start of combustion has been derived from the heat release curves in Fig. 3. The exhaust NO concentration levels are indicated as well.

3.2. Fuel spray characterization

Time-resolved (vapor) spray penetration was measured in the EHPC by means of high-speed Schlieren imaging. A typical frame taken from the high-speed movie is shown in Fig. 7. The strong background density fluctuations are a consequence of the precombustion. They move much more slowly than the fuel jet, and in the analysis they are dealt with by interpolating the spray edge across each "dark spot," in order to obtain a reliable measure for the spray angle and penetration depth. Based on these results, the average spray full angle was evaluated as $\theta_{\mathrm{spray}} = 18°$. Following the approach by Naber and Siebers, for a given spray angle, the measured penetration length can be correlated with the average equivalence ratio (mass-averaged value across the spray cross-sectional area) at the spray tip [10]. For a quasi-steady spray this penetration curve also corresponds to the dependence of this average equivalence ratio on the distance to the injector. Both the spray penetration and the corresponding equivalence ratio are shown in Fig. 8 for the four injection timings we investigated. For each curve the start of combustion is indicated as well, revealing that on average the jet is rather fuel-rich when the mixture ignites: $\Phi \approx 1.5$ for all curves except the one for 18° bTDC when $\Phi \approx 1.2$.

The relatively high equivalence ratios at the start of combustion suggest that the initial, premixed combustion is too fuel-rich for significant thermal NO formation to take place, as the latter requires near-stoichiometric equivalence ratios ($0.8 \leqslant \Phi \leqslant 1.0$) [30]. Prompt NO formation, however, may occur in rich zones with equivalence ratios up to $\Phi \approx 1.8$ and may play some role in the observed NO concentrations.

Fig. 8 also indicates that the combustion starts with the spray tip close to the piston bowl rim. For the injection at 18° bTDC, the jet has just reached the bowl rim when ignition occurs, whereas for the other injection timings, the spray tip is still 6–7 mm away from the rim. This is in agreement with the high-speed combustion movies showing the first combustion luminosity (i.e., soot incandescence) at the edges of the piston window.

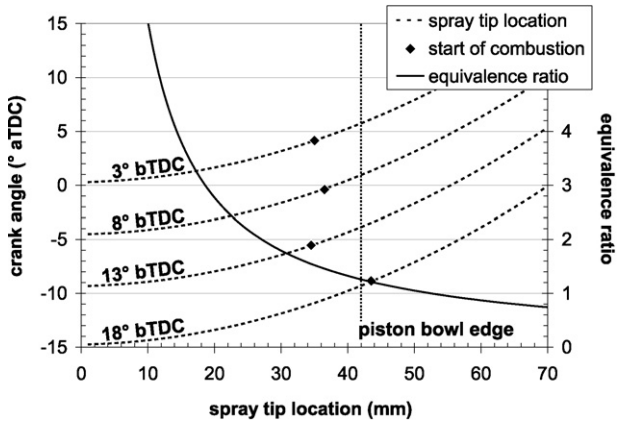

Fig. 8. Relation between spray penetration and crank angle, and equivalence ratio as a function spray tip location. The start of injection is indicated in each penetration curve, as well as the piston bowl diameter.

3.3. NO LIF measurements

The *in-cylinder* NO concentrations are shown in Fig. 9 as a function of crank angle and injection timing. The data points are phase-averaged over 20 cycles, and the error bars include both the processing uncertainties and cycle-to-cycle fluctuations. Similarly to the exhaust concentration, the in-cylinder NO concentration increases almost linearly when the fuel injection is advanced. All NO curves have very similar shapes, varying only in the moment of first NO and in amplitude. The peak concentrations range from 1500 ppm (SoI = 3° bTDC) to values just over 5000 ppm (SoI = 18° bTDC). Typically, the peak concentration is approximately nine times higher than the asymptotic value reached by 130° aTDC.

Generally, the first significant NO LIF appears ∼5° after the start of combustion. Given the facts that (1) the initial, premixed combustion takes place within the fuel spray boundaries [11] and that (2) the laser beam is 14 mm away from the spray axis, the probe location may be too far away to detect any (prompt) NO formed during the initial premixed combustion, unless this prompt NO is convected towards the probe location. Such transport cannot be excluded; with a swirl ratio of 1.8 this would require 5°–7°, which is only slightly longer than the observed delay of 5°. Nevertheless, in the latter case a considerable dilution of the transported NO would be expected.

On the other hand, the high-speed combustion movies show that the moment when the first NO is detected coincides within 0.5° CA with the moment when luminous soot[2] is first observed at the probe location. This is shown in Fig. 10. The first appearance of the diffusion flame in the probe volume is also indicated in Fig. 9. This implies that the observed

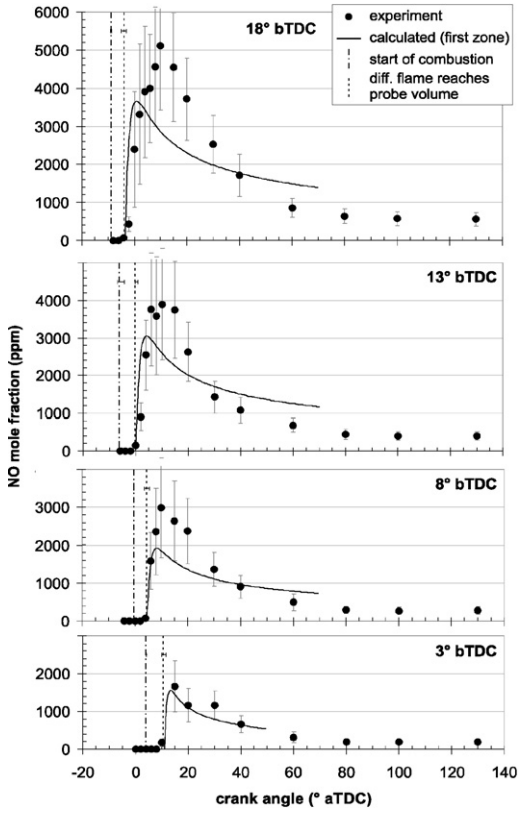

Fig. 9. Local NO mole fractions (phase-averaged over 20 cycles) as a function crank angle and injection timing. The error bars contain cyclic variations (10–30%) as well as the uncertainties in all processing steps (attenuation correction and p, T dependence). The solid curves are explained in Section 3.4.

[2] According to Dec's conceptual model, the luminous soot is representative of the diffusion flame [11].

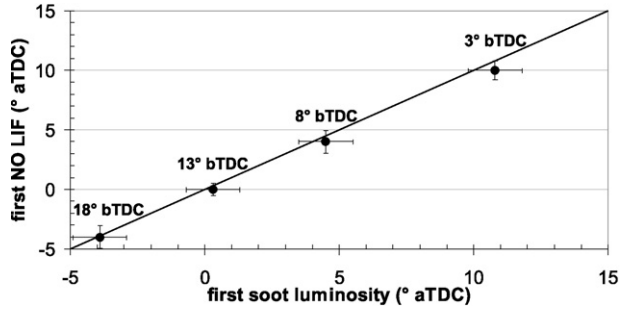

Fig. 10. The moment of first detected NO vs the moment of first soot luminosity in the probe volume. The straight line assumes equal moments of first NO LIF and first soot luminosity.

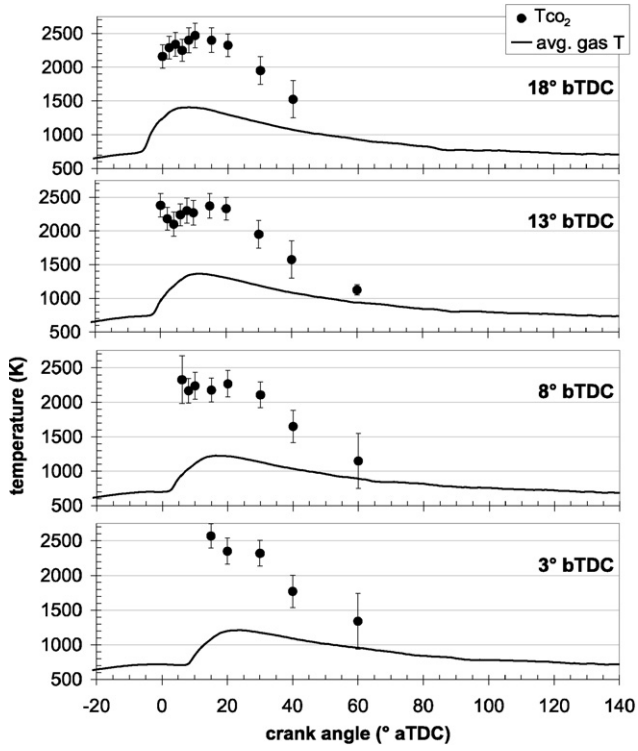

Fig. 11. Local temperatures, based on CO_2 and O_2 absorption spectra. The spatially averaged gas temperature (derived from the pressure curve) is shown for comparison.

NO is (primarily) due to the thermal NO formation mechanism; the arrival of the diffusion flame at the probe location quickly raises the local temperature above the threshold for thermal NO formation (1700–1800 K), leading to a sudden increase of the NO concentration, in agreement with the NO LIF results. The sudden temperature increase is confirmed by experimental temperature values derived from CO_2 absorption spectra, shown in Fig. 11. Note that the measured peak temperatures do not vary significantly with SoI, in contrast to the peak NO concentrations of Fig. 9.

From 40° aTDC onwards, all NO concentration curves decay at the same rate. This is illustrated in Fig. 12, where all curves are normalized at 130° aTDC. By 40° aTDC the combustion has ceased for all four injection timings. Moreover, the local temperature has dropped below 1800 K, and no significant NO formation is to be expected. As a consequence, the concentration decay is attributed to mixing of the combustion products with unburnt gases until a stable value is reached. This process is identical for all four experimental conditions.

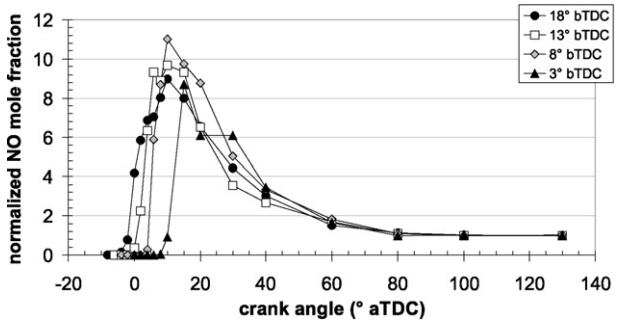

Fig. 12. Normalized NO mole fractions during the combustion stroke, based on the data in Fig. 9.

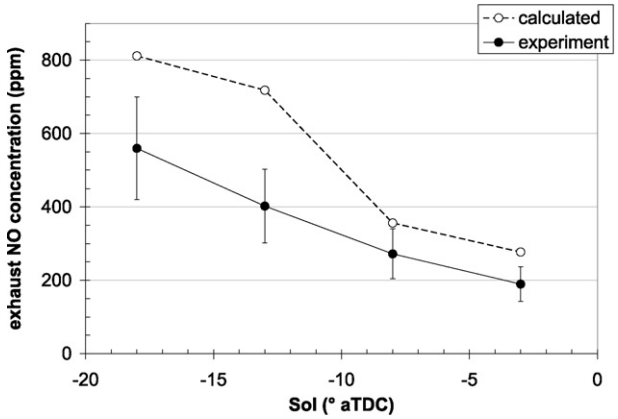

Fig. 13. Calculated and experimental exhaust NO concentration vs SoI.

3.4. Calculated NO formation

Fig. 13 demonstrates that the NO formation calculations are in reasonable agreement with the exhaust concentration measurements. Fig. 14 shows the calculated NO molar fraction in all product zones as a function of crank angle. The first zone is formed when the premixed burn spike of the heat release rate has its maximum, which is a crude estimate of the onset of the diffusion flame (according to the combustion movies, the luminous diffusion flame appears even 1°–2° CA earlier). Every following 1.0°, a new product zone is formed. The observed decrease in the NO concentration per zone is caused by (1) a shifting of the H–C–O equilibrium as a result of the varying temperature and leading to destruction of some of the earlier formed NO and (2) by diluting the zone with newly entrained fresh air.

For all four data sets, the start of the first zone is very close to the moment the diffusion flame appears in the laser probe volume. For instance, for the SoI = 18° bTDC measurements, the first zone starts at 3.5° bTDC, as compared to 3.9° bTDC for the appearance of the flame; for the SoI = 8° bTDC series these values are both 4.5° aTDC. Therefore, in line with the earlier observations (Section 3.3), the first zones are considered representative for the initial part of the experimental concentration curve. In reality, of course, the probe volume will see a mixture of such zones.

For SoI = 18° bTDC, a peak concentration around 3600 ppm is calculated, in reasonable agreement with the experimental 5100 ± 1700 ppm. The agreement between experiment and calculation is of similar quality for the other injection timings. Here it should be noted that the model does not contain any adjustable parameters, but just calculates the expected amount of NO on the basis of the measured rate of heat release and spray characteristics. The calculated NO concentration of the first zone is also shown in Fig. 9 for easy comparison of the peak values. The difference in the decay rate between experimental and numerical concentration histories might be related to the fact that the zones move past the probe volume, so that the first zone is only representative for the initial part of the measured concentration history. Another explanation might be the air entrainment model: the model by Naber and Siebers is only applicable to a quasi-steady spray and will only be an ap-

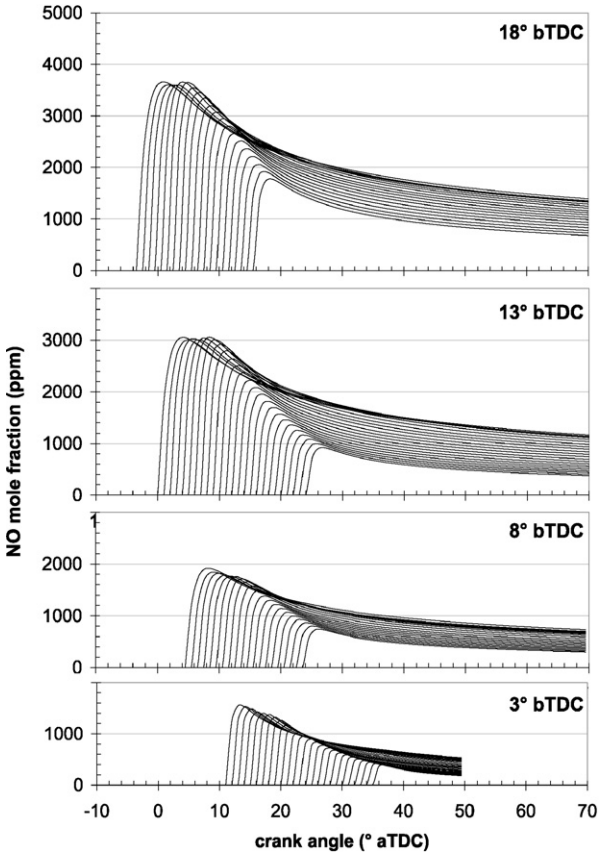

Fig. 14. NO concentration in each product zone vs crank angle.

proximation of the mixing processes in the diffusion flame.

The calculations show that once the diffusion flame has arrived at the probe volume, *local* thermal NO formation is fast enough to account for a significant fraction of the observed NO. Since the observed NO concentrations are nevertheless systematically higher than the calculated ones, it cannot be excluded that transport of earlier formed NO (not modeled) might play a role as well.

4. Summary and conclusions

We have presented local in-cylinder NO concentration histories, both measured and calculated, for various injection timings in a diesel engine. Based on a combination of these data with additional experiments, such as high-speed visualization of the combustion and Schlieren imaging of the fuel spray, we feel it justified to draw the following conclusions.

The well-known trend of increasing exhaust NO emissions with advancing injection timing is also reflected in the in-cylinder concentration histories. In fact, all concentration histories are quite similar, varying only in onset and peak amplitude. In each case, the maximum concentration in the probe volume is around nine times the concentration reached by the end of the stroke. Apparently, only a small part of the combustion chamber is responsible for the bulk of the NO that is produced. This is of course in line with the engine operating at low load during the experiments, resulting in a low overall equivalence ratio.

The same NO vs SoI trend is observed in our numerical data. The agreement between experiment and calculation is qualitatively good. This suggests that the observed NO is caused by *local* thermal NO formation rather than transport. However, the experimental values are systematically somewhat higher than the calculated ones. Therefore, it cannot be excluded that NO formed during the premixed combustion is transported towards the probe location. The time needed for this transport is very close to the observed delay between the start of combustion and the first NO LIF appearance, suggesting that the prompt and/or N_2O mechanisms may indeed contribute to the observed local NO concentrations.

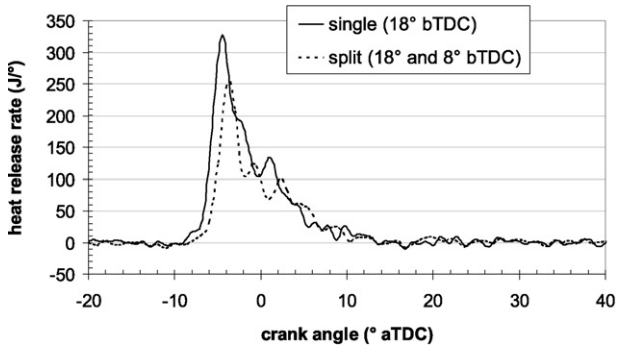

Fig. 15. Rate of heat release for a single (SoI = 18° bTDC) and a split fuel injection ($SoI_1 = 18°$ bTDC, $SoI_2 = 8°$ bTDC).

Our present experimental data do not allow an accurate investigation of the prompt NO mechanism. The data in Fig. 8 show that the initial combustion is too fuel-rich for significant thermal NO formation. Therefore, further in-cylinder NO LIF experiments, moving the probe volume toward the premixed burn region and combined with more accurate local temperature measurements (e.g., by vibrational thermometry [31]), would be elucidating. Thus far, measurements with the laser beam directed through a fuel spray suffered from severe window fouling, and the current probe location was preferred for further experiments. Previous "through spray" NO LIF measurements in the same research engine, [9] but with the original cam-driven fuel injection, showed significant NO fluorescence during the premixed burn phase, at temperatures too low for thermal NO formation.

All concentration curves decay at the same rate from 40° aTDC onwards. This is attributed to transport/mixing, since by that time the combustion has finished and local temperatures are too low for significant thermal NO formation. This is also confirmed by the calculations, that show a constant NO mass after 40° aTDC. Considering the large impact of transport on the local NO concentration, a more detailed comparison of experimental and numerical data will only be possible either by (1) by extending the fluid dynamics of the numerical simulations, or (2) by two-dimensional LIF imaging of a larger fraction of the combustion chamber, measuring the total NO density [3]. The latter would require two-dimensional attenuation corrections as well as a local temperature map, two issues that will bring new experimental challenges.

Acknowledgment

This research is supported by the Technology Foundation STW, applied science division of NWO and the technology programme of the Dutch Ministry of Economic Affairs.

Appendix A. Split fuel injection

In addition to the four injection strategies, the effect of split fuel injection was investigated as well. For the latter, 30 mg of fuel was injected twice, at 18° bTDC and at 8° bTDC, leaving ∼5° between the two injections.

Fig. 15 shows that the maximum rate of heat release is significantly reduced by the split injection. Due to the increased entrainment of fresh air, and due to cooling by the late second injection, the combustion temperatures are lower, and as a result the thermal NO formation is reduced. This was also observed experimentally, the exhaust NO concentration being reduced from 560 ppm (single injection at 18° bTDC) to 412 ± 80 ppm. The in-cylinder concentrations are shown in Fig. 16. The concentration history for the single injection at 18° bTDC is shown for comparison.

Interestingly, the peak concentration is only ∼5 times higher than the final concentration, as opposed to the factor of 9 for the single injections. This is most likely a consequence of the improved air entrainment (during combustion), lowering the peak temperatures and diluting the combustion products. After 40° aTDC, when the combustion has ended, the concentration history follows the same decay as the histories for the single injections.

Appendix B. Exhaust calibration in skip-fired operation

The time response of the exhaust gas analyzer, used for calibration of the in-cylinder NO measurements, is insufficient to resolve the NO concentration levels of every individual engine cycle. Thus, only averages can be obtained. By skip-firing the measurement cylinder (at a ratio of 1:35), the exhaust gas of a fired cycle is strongly diluted, with the compressed air resulting from adjacent motored cycles. If the exhaust gas were measured isokinetically (i.e.,

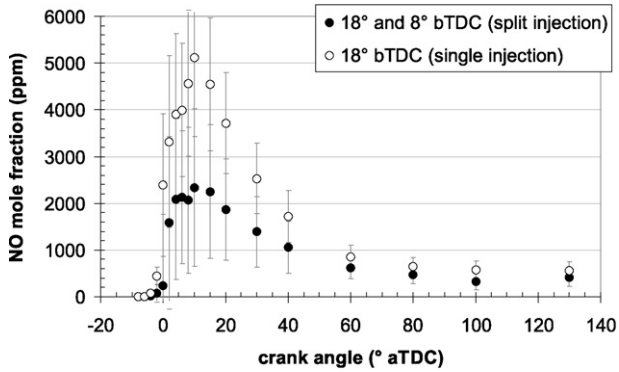

Fig. 16. Local NO mole fractions during the combustion stroke, for single and split injections. The start of each injection is indicated in the upper right corner.

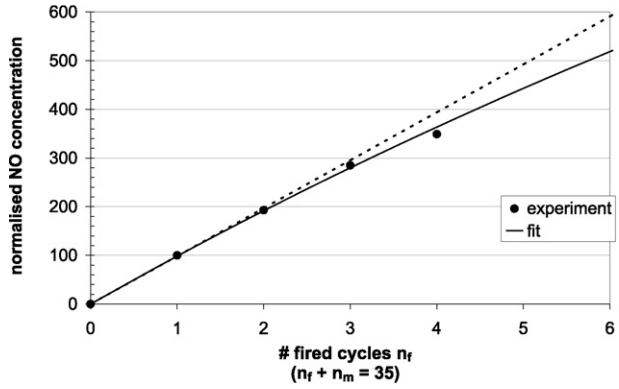

Fig. 17. Measured exhaust NO concentration [32] as a function of the number of fired cycles per 35. The dashed straight line assumes a linear dependence; the curved solid line is based on a bias of $\xi = 2$.

equal sampling speed for all cycles), the NO concentration from a fired cycle would simply be 35 times as high as the average concentration. In practice, it was observed that the hot exhaust from fired cycles is sampled more easily, thus biasing the average concentration. This is demonstrated in Fig. 17, showing a sublinear dependence of the analyzer reading as a function of fired cycles per 35. The fit is given by the equation

$$[\mathrm{NO}]_{\mathrm{meas}}(n_\mathrm{f}) = \frac{\xi n_\mathrm{f}[\mathrm{NO}]_{\mathrm{actual}}}{n_\mathrm{m} + \xi n_\mathrm{f}}, \tag{B.1}$$

with $[\mathrm{NO}]_{\mathrm{meas}}$ the measured NO concentration, $[\mathrm{NO}]_{\mathrm{actual}}$ the actual NO concentration from a fired cycle, n_f and n_m the number of fired and motored cycles, respectively, and ξ the "bias" towards a fired cycle. The best fit is obtained with $\xi \approx 2$, indicating that a skip-fired exhaust measurement overestimates the NO concentration from a fired cycle by approximately a factor of two. Obviously, for $n_\mathrm{f} = 35$ (and $n_\mathrm{m} = 0$), one would directly measure the NO concentration of a fired cycle. In general, the higher n_f, the more accurate the value of ξ. In practice, n_f is restricted to low values in order to prevent damage to the nonlubricated measurement cylinder.

References

[1] Th.M. Brugman, R. Klein-Douwel, G. Huigen, E. van Walwijk, J.J. ter Meulen, Appl. Phys. B 57 (1993) 405–410.

[2] Th.M. Brugman, G.G.M. Stoffels, N.J. Dam, W.L. Meerts, J.J. ter Meulen, Appl. Phys. B 64 (1997) 717–724.

[3] J.E. Dec, R.E. Canaan, SAE Tech. Pap. Series, no. 980147, 1998.

[4] G.G.M. Stoffels, E.J. van den Boom, C.M.I. Spaanjaars, N. Dam, W.L. Meerts, J.J. ter Meulen, J.C.L. Duff, D.J. Rickeard, SAE Tech. Pap. Series, no. 1999-01-1487, 1999.

[5] F. Hildenbrand, C. Schulz, J. Wolfrum, F. Keller, E. Wagner, Proc. Combust. Inst. 28 (2000) 1137–1143.

[6] E.J. van den Boom, P.B. Monkhouse, C.M.I. Spaanjaars, W.L. Meerts, N.J. Dam, J.J. ter Meulen, in: V.I. Vlad (Ed.), ROMOPTO 2000, Sixth Conference on Optics, Proc. SPIE, vol. 4430, 2001, pp. 593–606.

[7] F. Hildenbrand, C. Schulz, F. Keller, G. König, E. Wagner, SAE Tech. Pap. Series, no. 2001-01-3500, 2001.
[8] K. Verbiezen, R.J.H. Klein-Douwel, A.J. Donkerbroek, A.P. van Vliet, W.L. Meerts, N.J. Dam, J.J. ter Meulen, Appl. Phys. B 83 (2006) 155–166.
[9] K. Verbiezen, R.J.H. Klein-Douwel, A.P. van Vliet, W.L. Meerts, N.J. Dam, J.J. ter Meulen, Proc. Combust. Inst. 31 (2006) 765–773.
[10] J.D. Naber, D.L. Siebers, SAE Tech. Pap. Series, no. 960034, 1996.
[11] J.E. Dec, SAE Tech. Pap. Series, no. 970873, 1997.
[12] P.F. Flynn, R.P. Durrett, G.L. Hunter, A.O. zur Loye, O.C. Akinyemi, J.E. Dec, C.K. Westbrook, SAE Tech. Pap. Series, no. 1999-01-0509, 1999.
[13] J.B. Heywood, Internal Combustion Engine Fundamentals, McGraw–Hill, Singapore, 1988.
[14] R.J.H. Klein-Douwel, M. Douch, L.M.T. Somers, W.A. de Boer, R.S.G. Baert, Proc. European Combustion Meeting, Orléans, France, 2003.
[15] P.J.M. Frijters, R.J.H. Klein-Douwel, S.S. Manski, L.M.T. Somers, R.S.G. Baert, Proc. European Combustion Meeting, Louvain-la-Neuve, Belgium, 2005.
[16] K. Verbiezen, Quantitative NO measurements in a diesel engine, Ph.D. thesis, Radboud University, Nijmegen, The Netherlands, 2007, available from http://webdoc.ubn.ru.nl/mono/v/verbiezen_k/quannomei.pdf.
[17] M.D. diRosa, K.G. Klavuhn, R.K. Hanson, Combust. Sci. Technol. 118 (1996) 257–283.
[18] D. Stepowski, Proc. Combust. Inst. 23 (1990) 1839–1846.
[19] M. Versluis, N. Georgiev, L. Martinsson, M. Aldén, S. Kröll, Appl. Phys. B 65 (1997) 411–417.
[20] G.G.M. Stoffels, S. Stoks, N. Dam, J.J. ter Meulen, Appl. Opt. 39 (2000) 5547–5559.
[21] V. Sick, B.D. Stojkovic, Appl. Opt. 40 (2001) 2435–2442.
[22] C. Schulz, J.B. Jeffries, D.F. Davidson, J.D. Koch, R.K. Hanson, Proc. Combust. Inst. 29 (2002) 2735–2742.
[23] K. Verbiezen, A.P. van Vliet, W.L. Meerts, N.J. Dam, J.J. ter Meulen, Combust. Flame 144 (2006) 638–641.
[24] J.B. Jeffries, C. Schulz, D.W. Mattison, M.A. Oehlschlaeger, W.G. Bessler, T. Lee, D.F. Davidson, R.K. Hanson, Proc. Combust. Inst. 30 (2005) 1591–1599.
[25] W.G. Bessler, C. Schulz, V. Sick, J.W. Daily, LIFSim: A versatile modeling tool for nitric oxide LIF spectra, Chicago, 2003, http://www.lifsim.com.
[26] S.L. Plee, J.P. Ahmad, J.P. Myers, G.M. Faeth, Proc. Combust. Symp. 19 (1982) 1495–1502.
[27] K.J. Wu, R.C. Peterson, SAE Techn. Pap. Series, no. 861566, 1986.
[28] S. Gordon, B.J. McBridge, Computer program for the calculation of complex chemical equilibrium compositions with applications; I. Analysis, NASA Reference Publication 1311, 1994.
[29] G.P. Smith, D.M. Golden, M. Frenklach, N.W. Moriarty, B. Eiteneer, M. Goldenberg, C.T. Bowman, R.K. Hanson, S. Song, W.C. Gardiner Jr., V.V. Lissianski, Z. Qin, GRI mech 2.11, Technical report, 2000; http://www.me.berkeley.edu/gri_mech.
[30] J.A. Miller, C.T. Bowman, Prog. Energy Combust. Sci. 15 (1989) 287–338.
[31] W.G. Bessler, F. Hildenbrand, C. Schulz, Appl. Opt. 40 (2001) 748–756.
[32] G.J. Schoonderbeek, Emissiemeting aan de uitlaat van een dieselmotor, Graduation report, University of Nijmegen, 2002.